RSC Advances

PAPER

View Article Online
View Journal | View Issue

Cite this: *RSC Adv.*, 2026, **16**, 26334

Synergistic integration of mixed metal phosphate and poly(1*H*-pyrrole) for high-performance asymmetric supercapacitor

Malek Ali,[a] Junaid Khan,[*bc] Sarah S. Albalawi,[d] M. Ahmed[e] and Asif Mahmood[*f]

Received 24th March 2026
Accepted 5th May 2026

DOI: 10.1039/d6ra02421a

rsc.li/rsc-advances

Transition metal phosphates offer attractive charge-storage capability and environmental stability, yet their practical use is limited by modest energy density and durability in electrolyte-rich conditions. Here, a zinc-incorporated nickel–cobalt phosphate (MMP) was synthesized hydrothermally and integrated with poly(1*H*-pyrrole) (physical mixing approach). The incorporation has enticingly enhanced electrical conductivity, ion-transport kinetics, and structural robustness. The optimized MMP-PPY2 (25 wt% poly(1*H*-pyrrole)), composite achieved high specific capacity of 1347.6C g^{-1} at 1.2 A g^{-1}. An asymmetric supercapacitor assembled using MMP-PPY2 as the positive electrode and activated carbon as the negative electrode delivered an energy density of 104.9 Wh kg^{-1} and a power density of 11 900 W kg^{-1}, retaining 97.9% of its capacity after 4000 cycles. These results highlight the strong potential of phosphate-based hybrid composites for high-performance asymmetric supercapacitor applications.

1. Introduction

The increasing need for portable electric devices and electric cars is driving widespread scientific efforts to develop improved energy storage solutions that are cost-effective, safe, and highly efficient.[1,2] Among the diverse options, supercapacitors have garnered substantial attention due to their rapid charge–discharge capabilities, high power density, excellent cycle life, and superior operational safety.[3–5] However, their low Specific energy (E_s) remains a critical bottleneck that hinders their broader commercialization.[6] To address this limitation, hybrid supercapacitors which integrate battery-type electrodes with electric double-layer capacitors (EDLCs)—have emerged as a promising solution. These devices combine the high energy density of battery grade materials with the power advantages and cycling stability of EDLCs, thereby offering a synergistic pathway toward enhanced performance.[7,8] Materials such as transition metal oxides, sulfides, chalcogenides, and conducting polymers exhibit superior energy densities compared to EDLC materials, yet often suffer from poor rate capability and conductivity, limiting their application.[9–12] In contrast, carbon-based materials are widely employed in EDLCs for their ability to store charge *via* electrostatic adsorption, providing excellent power density and cycling stability, though at the cost of reduced energy density.[13,14]

Developing high-performance supercapacitors thus necessitates the rational design and modification of battery-type electrode materials to overcome intrinsic limitations. In this regard, transition metal phosphates (TP) have received considerable attention due to their structural tunability, environmental benignity, and cost-effectiveness.[15] Their rich redox chemistry, arising from multiple accessible valence states (*e.g.*, Ni^{2+}/Ni^{3+} in Ni phosphate and Co^{2+}/Co^{3+} in Co phosphate), facilitates rapid and reversible faradaic reactions, thereby offering high theoretical capacities.[16,17] Despite these advantages, the practical performance of TMPs is hindered by several intrinsic limitations. First, their inherently low electrical conductivity restricts efficient electron transport and compromises rate capability. Second, sluggish ion diffusion—attributed to dense crystal frameworks and extended OH^- diffusion pathways—limits the effective utilization of active sites. Third, repeated charge–discharge cycling induces significant volume fluctuations, leading to structural degradation, particle pulverization, and rapid capacity decay.[15,18,19] As a result, pristine TMPs often exhibit suboptimal specific capacity and poor long-term cycling stability.

To address these limitations, extensive efforts have been devoted to compositional engineering and the rational design of hybrid architectures with functional materials.[20–23] Bimetallic Ni–Co phosphate has attracted particular attention due to its

[a]*Department of Aviation Science and Management, Faculty of Aviation Sciences, Amman Arab University, Amman 11953, Jordan*

[b]*Department of Physics, Government Postgraduate College No.1, Abbottabad, Khyber Pakhtunkhwa, Pakistan. E-mail: junaidkhan.nanotech@gmail.com*

[c]*Department of Higher Education, Archives and Libraries, Government of Khyber Pakhtunkhwa, Pakistan*

[d]*Department of Chemistry, College of Science, University of Jeddah, P.O. 80327, Jeddah 21589, Saudi Arabia*

[e]*Department of Computer Science, University College, Korea University, 145 Anam-ro, Seongbuk-gu, Seoul, 02841, South Korea*

[f]*Department of Chemical Engineering, College of Engineering, King Saud University, Riyadh 11421, Saudi Arabia. E-mail: ahayat@ksu.edu.sa*

comparatively improved electrical conductivity, abundant redox-active sites, and the synergistic interaction between Ni and Co centers. This bimetallic synergy promotes enhanced charge transfer kinetics and delivers superior electrochemical performance relative to monometallic analogues.[15,24] Nevertheless, it still suffers from persistent challenges (structural instability during prolonged cycling and sluggish reaction kinetics).[25–27] To further optimize their performance, the incorporation of a third metal ion—such as zinc (Zn)—into the host lattice has emerged as an effective strategy. Zn incorporation can modulate the electronic structure, introduce additional electrochemically active sites, and improve structural robustness, thereby enhancing rate performance and cycling stability.[28] In a recent work, Zn incorporated Co–Mn phosphate was reported with refined morphology and 2.53 times improved storage capability as compared to the bimetallic version.[29] Stability potential and rate capability were also reported to be improved. However, despite these improvements, Zn doping alone is insufficient to fully mitigate critical issues such as conductivity, volume expansion during repeated charge–discharge processes, and restricted ion diffusion pathways.[30] These unresolved limitations continue to impede the realization of high-performance and durable energy storage devices.

A variety of approaches have been explored to overcome these limitations. A particularly effective strategy is the incorporation of suitable dopants, such as conducting polymers (*e.g.*, polythiophene, poly(1*H*-pyrrole), and polyaniline) or carbon-based allotropes. Such modifiers suppress agglomeration of the active material and simultaneously enhance the electrochemical performance of TP-electrodes by improving electrical conductivity, facilitating ion diffusion, and extending long-term cycling stability.[18,31–33] Unlike rigid carbon allotropes such as graphene or carbon nanotubes, which tend to aggregate and provide only electric double-layer storage, conducting polymers like poly(1*H*-pyrrole) (PPy) offer multiple synergistic advantages.[34] A synergistic combination of PPy and Li–Fe phosphate was reported by Y. Wang.[35] The composite was found with improved conductivity and accelerated diffusion, leading to better performance. In another recent study PPy incorporation in nickel ferrite boosted the specific capacity three times[36] with PPy acting as a conductive support and redox active supplement. Owing to its intrinsically high conductivity, porous and flexible morphology PPy establishes a continuous electron-transporting network when composited with other electrode materials.[37–39] This creates interconnected pathways that improve ion mobility to and from the redox-active sites. The flexible polymer chains of PPy also act as a mechanical buffer, absorbing volume expansion and contraction during repeated charge–discharge cycles, thereby preventing particle pulverization and structural degradation—a critical factor for achieving long-term cycling stability.[40–42] The presence of PPy also increases the electrochemically active surface area by forming a thin coating around the active particles, thereby exposing more redox-active sites and boosting specific capacity. Furthermore, PPy contributes its own pseudocapacitive behavior to the overall charge storage process, enhancing the total capacitance and rate capability of the electrode.[43] Collectively, these properties make PPy a superior additive for balancing high specific capacity, rate capability, and cycling stability in phosphate-based supercapacitor electrodes.

Motivated by these considerations, we herein report a rationally designed hybrid electrode architecture comprising Zn-doped Ni–Co phosphate (MMP) integrated with PPy with their native structure preserved. The incorporation of Zn is intended to fine-tune the electronic structure of the Ni–Co phosphate matrix, thereby increasing the density of electrochemically accessible redox-active sites and facilitating accelerated faradaic charge-transfer kinetics. Subsequent integration with PPy effectively addresses the fundamental limitations of pristine metal phosphates. In particular, (i) the intrinsically low electronic conductivity is substantially enhanced *via* the formation of a percolative conductive polymer network; (ii) sluggish ion transport is alleviated through the development of a hierarchically porous, sponge-like morphology that promotes efficient electrolyte infiltration and ion diffusion; and (iii) structural degradation associated with repetitive volumetric fluctuations during prolonged cycling is mitigated by the mechanically compliant PPy matrix, which functions as a stress-buffering layer to suppress particle pulverization and interfacial delamination. By systematically optimizing the PPy content (15, 25, and 35 wt%), an optimal synergistic composition was identified and subsequently implemented in the assembly of an asymmetric supercapacitor device. Collectively, this work delineates a coherent, design-driven strategy to effectively overcome the intrinsic shortcomings of transition metal phosphates, thereby enabling their deployment in next-generation high-performance asymmetric supercapacitor systems.

2. Experimental section

2.1. Materials

All chemicals employed in this study were of analytical grade and used as received without any further purification. Nickel(II) nitrate hexahydrate, cobalt(II) nitrate hexahydrate, and zinc(II) nitrate hexahydrate served as the primary metal precursors. Sodium phosphate was employed as the phosphate source, while hydrazine hydrate acted as a reducing agent. Ammonium persulfate ($(NH_4)_2S_2O_8$) was used as an oxidant for poly(1*H*-pyrrole) (PPy) synthesis. Conductive additives included acetylene black (AB) and activated carbon (AC), and polyvinylidene fluoride (PVDF) was used as a binder. NMP functioned as the solvent for slurry preparation. Ethanol and acetone were employed as cleaning and washing agents. All chemicals were purchased from Sigma-Aldrich.

2.2. Synthesis of mixed metal phosphate (MMP)

The synthesis of Zn-incorporated nickel–cobalt phosphate was achieved *via* a hydrothermal route involving multiple preparatory steps. Initially, 0.686 g of nickel nitrate, 0.635 g of cobalt nitrater, and 0.234 g of zinc nitrate were dissolved in 35 mL of DI water under constant magnetic stirring to prepare the metal nitrate precursor solution (Solution A). In parallel, 0.343 g of sodium phosphate was dissolved in 15 mL of DI water with

continuous stirring for 15 minutes to form Solution B. Solution A was gradually introduced into Solution B using a dropwise method while the mixture was agitated intensely to guarantee a consistent blend. Following this, 3 mL of hydrazine hydrate ($N_2H_4 \cdot xH_2O$, 50–60%) was added to initiate the reduction process and encourage crystal growth, after which stirring continued for another hour. All of the aforementioned procedures were carried out at ambient temperature. The resulting uniform suspension was then placed in an autoclave and underwent a hydrothermal reaction at 160 °C for a full day. The solid product collected from this process was meticulously cleaned. Ultimately, the refined material was desiccated in a vacuum oven at 75 °C for 10 hours to produce the final mixed metal phosphate (MMP) composite material with corresponding composition of $Zn_{0.35}$-Ni_1-Co_1 phosphate.

2.3. Synthesis of poly(1*H*-pyrrole) (PPy)

Poly(1*H*-pyrrole) (PPy) was produced through a chemical oxidative polymerization method. The process began by dissolving 34.230 g ammonium persulfate ($(NH_4)_2S_2O_8$) as an oxidant in 100 mL of deionized water (0.15 molar solution). This solution was stirred continuously for 15 minutes while being cooled to 0 °C to maintain a uniform reaction environment. Next, 0.15 mol of pyrrole monomer (10.4 mL equivalent to 10.064 g) was introduced drop by drop into the oxidant solution with ongoing agitation (equal monomer: oxidant used). The ammonium persulfate solution serves as the oxidant and dopant.[44,45] The polymerization was allowed to proceed under constant stirring for 16 hours, during which a black precipitate slowly formed, confirming the generation of PPy. The initial pH of the APS solution in deionized water was measured to be approximately 3.5. Upon completion of the polymerization, the pH of the filtrate decreased to 1.8. This significant drop is consistent with the polymerization mechanism, which produces H^+ ions as a byproduct. The solid product was then isolated *via* vacuum filtration and rinsed extensively. The final PPy material, labeled PPY, was obtained after drying the purified polymer in an oven at 70 °C for 14 hours.

2.4. Preparation of composite

To incorporate PPy into the mixed metal phosphate (MMP) matrix, a physical mixing strategy employing mechanical stirring (Magnetic stirrer (IKA C-MAG HS 7)) coupled with ultrasonication was adopted. In a typical procedure, 1.0 g of MMP was dispersed in 30 mL of deionized water. The suspension was stirred magnetically at 300 rpm for 3 hours at ambient temperature (25 ± 2 °C), followed by ultrasonication for 30 minutes in a bath sonicator (40 kHz, 100 W) to ensure complete de-agglomeration and uniform dispersion of the MMP nanoflakes. Subsequently, poly(1*H*-pyrrole) (PPy) powder was added to the suspension in varying weight percentages: 15 wt% (MMP-PPY1), 25 wt% (MMP-PPY2), and 35 wt% (MMP-PPY3). The

Scheme 1 Schematic illustration of synthesis process.

mixture was further stirred at 300 rpm for 2 hours, followed by a final ultrasonication step of 15 minutes to promote intimate interfacial contact between the MMP and PPy components. Throughout the process, the temperature was maintained at 25 ± 2 °C. The resulting homogeneous dispersions were centrifuged at 5000 rpm for 10 minutes, and the solid residues were collected. The obtained material was washed and dried under vacuum at 70 °C for 8 hours. The final composites were labeled MMP-PPY1, MMP-PPY2, and MMP-PPY3 according to their PPy content. The whole synthesis process is represented schematically in Scheme 1.

The physical mixing approach was chosen over *in situ* polymerization to preserve the intrinsic conductivity and porous morphology of the pre-synthesized PPy, to avoid exposing the MMP framework to oxidative polymerization conditions, and to enable precise control over the polymer loading. Preliminary experiments confirmed that the described stirring and sonication parameters yield well-dispersed, agglomerate-free composites with reproducible electrochemical performance.[46]

2.5. Working electrode and device assembly

The electrode slurry was prepared by combining 80 wt% of the active material with 10 wt% acetylene black as a conductive additive and 10 wt% polyvinylidene fluoride as a binder, using *N*-methyl-2-pyrrolidone as the solvent. The mixture was stirred (magnetically) for 8 hours to achieve a uniform dispersion. Prior to slurry coating, nickel foam substrates (2 mm thick, 1 × 1 cm^2) were pretreated to remove surface oxides and organic residues. The foams were immersed in 3 M HCl solution and subjected to ultrasonication for 15 minutes. Subsequently, the foams were rinsed thoroughly with deionized water, followed by absolute ethanol, and then dried under vacuum at 60 °C for 12 hours. This cleaning procedure yields a clean, oxide-free surface that ensures strong adhesion of the active material and reproducible electrochemical performance.

The homogeneous slurry was then evenly coated onto the pretreated nickel foam substrates, which served as both the support and the current collector. After coating, the electrodes were dried at 70 °C for 9 hours to eliminate residual solvent and promote strong adhesion of the active layer.

Electrochemical measurements were conducted using a GAMRY ref. 3000 Potentiostat/Galvanostat in a 1 M KOH aqueous electrolyte. In asymmetric supercapacitor the mass of 3.50 mg cm^{-2} (active electrode material) was approximately employed for the battery type positive electrode, and for the AC anode, it was about 6.50 mg cm^{-2} (active electrode material) to ensure charge balancing and optimized performance of the device. The two electrodes were separated by a thin, porous membrane to facilitate ion transport while preventing electrical shorting. Finally, the assembled device was securely sealed to ensure proper packing and stability during electrochemical testing.

3. Results and discussion

3.1. Structural and morphological aspects

XRD analysis was performed to investigate the crystalline structure of the synthesized materials, and the corresponding diffraction patterns of all samples are presented in Fig. 1(a–e). For the MMP sample (Fig. 1(a)), distinct diffraction peaks were observed at 2θ values of 11.5°, 29.5°, 31.0°, 33.0°, 35.9°, 47.5°,

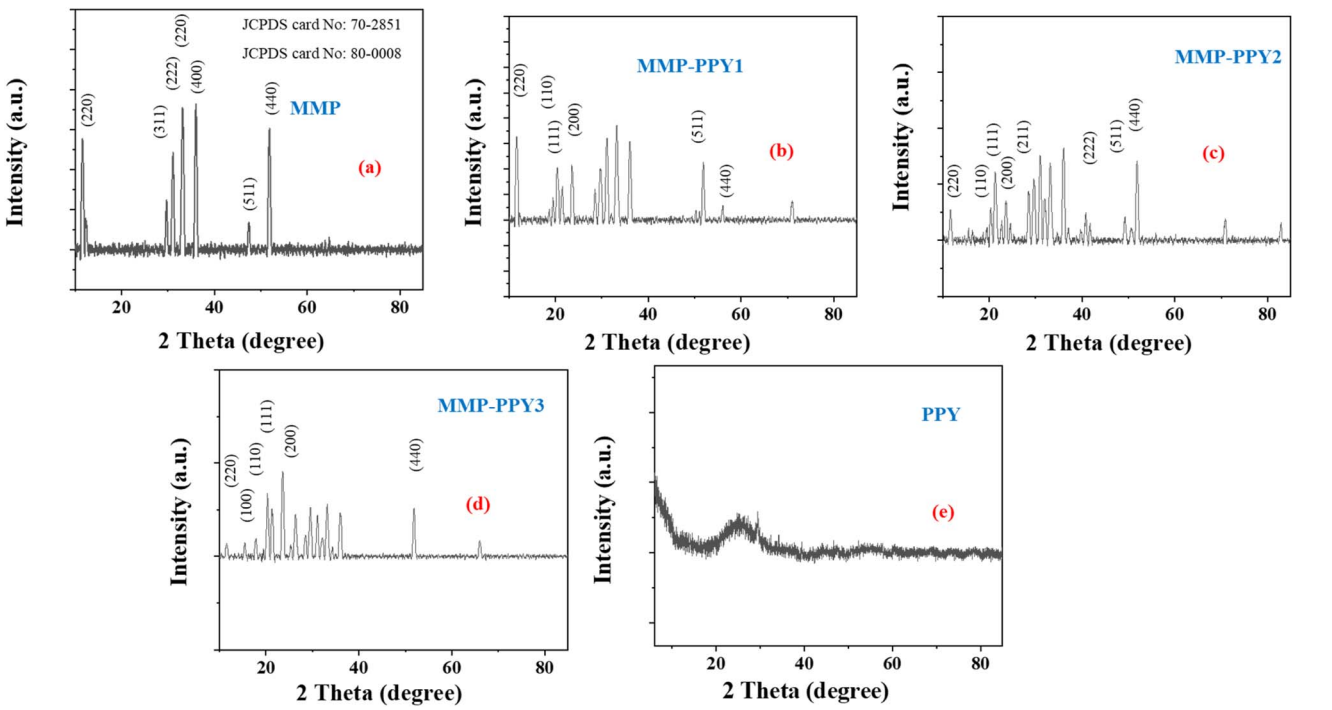

Fig. 1 (a–e) XRD pattern observed for MMP, MMP-PPY1, MMP-PPY2, MMP-PPY3, and PPY correspondingly.

and 51.7°, corresponding to the crystallographic planes (220), (311), (222), (400), (511), and (440), among others. These reflections are well indexed to JCPDS card no. 70-2851 (nickel cobalt phosphate) and no. 80-0008 (zinc phosphate),[47] confirming the successful formation of the mixed metal phosphate (MMP) phase with a spinel-type crystalline structure. For the PPy sample (Fig. 1(e)), a broad hump between diffraction angles of (2θ) 20–30° is observed, which corresponds to the presence of short-range ordering in the molecular arrangement of the amorphous polymeric matrix. The observed amorphous structure is in excellent agreement with previous reports[48,49] representing random stacking and irregular arrangement of polymer chains. In the composite samples (Fig. 1(b–d)), the XRD patterns display overlapping features of both MMP and PPy, confirming the successful integration of the polymer within the inorganic matrix. Notably, the MMP-PPY2 sample (Fig. 1(c)) exhibits the most balanced diffraction profile—the characteristic peaks of MMP remain visible, while a noticeable decrease in peak intensity and slight broadening are observed compared to pristine MMP. This indicates partial encapsulation of the crystalline MMP domains by PPy. The MMP-PPY1 (Fig. 1(b)) and MMP-PPY3 (Fig. 1(d)) exhibit relatively higher and lower peak sharpness, respectively, corresponding to lower and higher PPy contents. The well-defined peaks across all hybrid samples confirm that MMP retains its framework even after polymer incorporation. This structural arrangement is advantageous for electrochemical applications, as it facilitates ion transport and charge storage by combining the electrical conductivity of PPy with the structural stability of MMP.

The surface structures of the produced MMP were scrutinized using SEM, presented in Fig. 2. The undoped MMP sample (Fig. 2(a)) showed a structure composed of flakes, suggesting a constrained surface area and routes for ions movement. Conversely, the PPy dopant itself (Fig. 2(e)) revealed a rough, spongy structure made of connected spherical particles, which is a favorable configuration for rapid ion movement and faster reaction speeds. When 15% PPy was added to the MMP base (Fig. 2(b)), the polymer partially coated the surface (indicated by the highlight), but its spread was uneven and fragmented. With a higher PPy concentration of 25% (Fig. 2(c)), an ideal, highly porous framework developed, featuring a consistent and even layer of the polymer. This structural arrangement is anticipated to greatly boost electrical conductivity and ease ion access, leading to superior performance in electrochemical applications.[40] Nevertheless, when the PPy concentration was raised to 35% (Fig. 2(d)), it caused an over-saturation of the polymer. This led to the clumping of particles and the obstruction of the material's porous network. Such a change in structure is likely to impede the penetration of the electrolyte and reduce the material's overall electrochemical efficacy. Compared to all other tested formulations, the composite containing 25% PPy exhibited the most beneficial structural characteristics, achieving an optimal equilibrium of high electrical conductance, efficient ion movement, and extensive active surface area. These combined properties position it as the most suitable material for use in advanced supercapacitor electrodes.

To further validate the composite coverage of the MMP framework by the PPy, energy dispersive X-ray spectroscopy

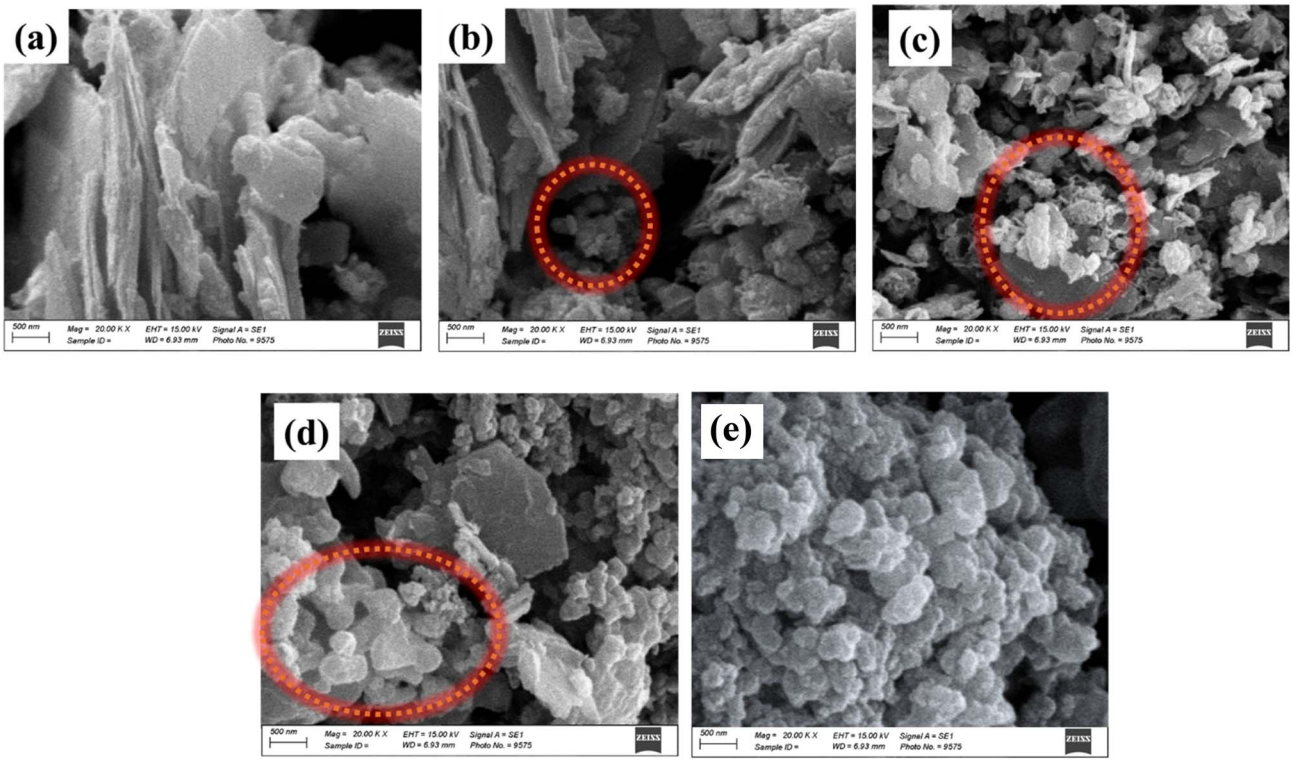

Fig. 2 (a–e) SEM image presenting surface morphology of for MMP, MMP-PPY1, MMP-PPY2, MMP-PPY3, and PPY correspondingly.

(EDS) elemental mapping was conducted for the optimized composite MMP-PPY2, as shown in Fig. S1 (SI). The elemental maps confirm the homogeneous distribution of Zn, Ni, Co, P, and O elements throughout the structure, indicating the uniform presence of the mixed metal phosphate phase. Simultaneously, distinct yet moderately dispersed signals of carbon (C) and nitrogen (N) are also observed, which originate exclusively from the poly(1*H*-pyrrole) (PPy) component. The relatively non-uniform and patchy distribution of C and N compared with the metallic elements reveals that PPy does not form a continuous coating but instead deposits locally on the MMP surface. This observation provides direct evidence of partial surface coverage, where the polymer layer encapsulates specific regions. Such a configuration ensures intimate interfacial contact between MMP and PPy, which is beneficial for facilitating charge transfer and ion diffusion during electrochemical processes.

Nitrogen adsorption–desorption isotherms and micropore size distributions for all samples are presented in Fig. 3(a). All samples exhibit Type I isotherm behavior, characterized by high N_2 uptake in the low relative pressure region ($P/P_0 < 0.1$), which is indicative of a microporous structure. The Brunauer–Emmett–Teller (BET) specific surface area of the pristine MMP sample was determined to be 567 $m^2 g^{-1}$. Upon incorporation of PPy, the specific surface area increases progressively: 716 $m^2 g^{-1}$ for MMP-PPY1, 784 $m^2 g^{-1}$ for MMP-PPY2, and 741 $m^2 g^{-1}$ for MMP-PPY3. The highest value observed for MMP-PPY2 (784 $m^2 g^{-1}$) is attributed to the synergistic effect of the conducting polymer network. Specifically, the introduction of PPy serves as a physical spacer that prevents the restacking and agglomeration of the MMP nanoflakes, thereby preserving interparticle porosity and exposing additional electroactive sites. Moreover, the porous and flexible nature of PPy itself contributes to the overall surface area by creating additional meso- and micropores within the composite matrix. The slight decrease in surface area for MMP-PPY3 (741 $m^2 g^{-1}$) suggests that excessive PPy content leads to partial pore blockage and particle clumping, consistent with the SEM observations (Fig. 2). The total pore volume follows a similar trend, increasing from ~0.22 $cm^3 g^{-1}$ for MMP to ~0.28 $cm^3 g^{-1}$ for MMP-PPY1 and reaching a maximum of ~0.33 $cm^3 g^{-1}$ for MMP-PPY2, followed by a slight decrease to ~0.30 $cm^3 g^{-1}$ for MMP-PPY3.

The FTIR spectra presented in Fig. 3(b–f) confirm the successful formation of Zn-doped Ni–Co phosphate (MMP), polypyrrole (PPY), and their composites. The spectrum of MMP exhibits a broad band around ~3400 cm^{-1} due to O–H stretching and a weak band near ~1630 cm^{-1} corresponding to H–O–H bending. Strong absorption bands in the range of 1200–900 cm^{-1} are assigned to PO_4^{3-} stretching vibrations, while bands below ~800 cm^{-1} arise from O–P–O bending and metal–oxygen (Ni–O, Co–O, Zn–O) vibrations, confirming the phosphate framework.

The observed absorption bands in Fig. 3(f) are in excellent agreement with previously reported spectra of polypyrrole.[50,51] Specifically, the peaks at 1554 cm^{-1} and 1474 cm^{-1} correspond to the fundamental stretching vibrations of the pyrrole ring. The bands at 1294 cm^{-1} and 1049 cm^{-1} are assigned to the in-plane =C–H bending vibrations, while the peak at 1196 cm^{-1} arises from the C–N stretching vibration of the pyrrole ring. The

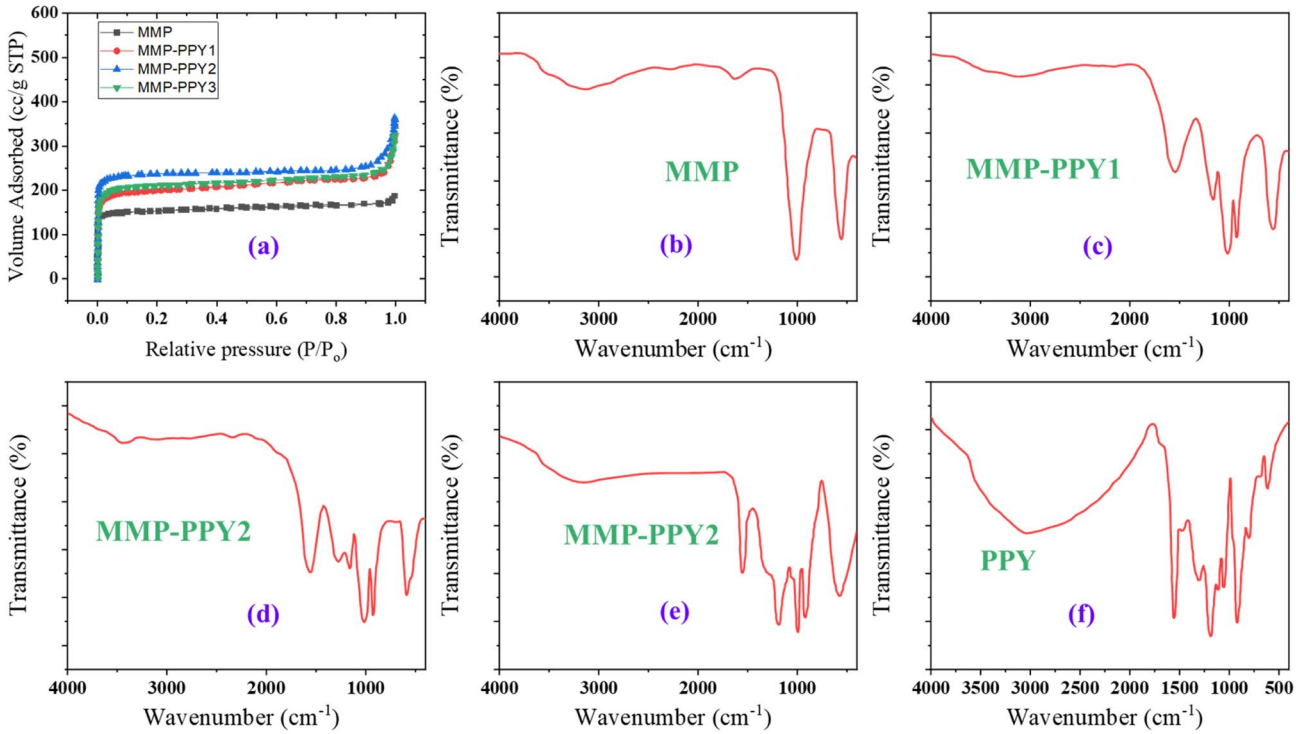

Fig. 3 (a) BET isotherm of synthesized MMP and MMP-PPY composites, (b–f) FTIR of all the samples correspondingly.

absence of any additional significant peaks confirms the successful polymerization of pyrrole without detectable side products. For the composites MMP-PPY1 (c), MMP-PPY2 (d), and MMP-PPY3 (e), both phosphate and PPY characteristic bands are observed. The PO_4^{3-} peaks are retained, while PPY-related bands appear with comparatively lower intensity due to the dominant MMP matrix. Slight shifts and changes in peak intensity are observed with increasing PPY content, suggesting strong interfacial interaction between MMP and PPY. These results confirm the successful incorporation of PPY into the Zn-$NiCo(PO_4)_2$ matrix, forming well-integrated hybrid composites.

The Raman spectrum of Zn-doped Ni–Co phosphate (Fig. S2) shows characteristic bands at ~310–377 cm^{-1} (metal–oxygen vibrations), ~484 cm^{-1} (O–P–O bending), and a strong peak at ~1058 cm^{-1} and a weak one at ~943 corresponds to the symmetric stretching of PO_4^{3-} groups, confirming the formation of a well-defined phosphate structure. The PPy spectrum exhibits prominent bands at ~1574 cm^{-1} (C=C stretching), ~1296 cm^{-1} (C–N stretching), and ~1190 cm^{-1} (C–H bending and ring deformation), indicating successful polymerization. In the Zn–$NiCo(PO_4)_2$/PPy composites, both phosphate and PPy features are preserved, with increasing intensity of PPy-related bands and slight peak shifts, suggesting strong interaction and successful integration of PPy within the phosphate matrix.

The TGA curves of Zn–$NiCo(PO_4)_2$, PPy, and their composites provide insight into the thermal stability and content. The pristine Zn–$NiCo(PO_4)_2$ shows minimal weight loss, indicating high thermal stability, whereas pure PPy exhibits significant degradation above ~300 °C due to polymer decomposition. The composite samples display intermediate behavior, combining the stability of the inorganic phase with the degradable nature of PPy. A systematic increase in weight loss is observed with increasing PPy content from MMP-PPY1 (15%) to MMP-PPY3 (35%), along with a corresponding decrease in residual mass at high temperature. Based on the residual weights, the PPy content in the composites is consistent with the intended composition, confirming the successful incorporation of PPy into the Zn–$NiCo(PO_4)_2$ matrix.

3.2. Electrochemical analysis in three cell configuration

3.2.1. Cyclic voltammetry (CV). CV was conducted for the synthesized electrode materials to evaluate their charge storage kinetics across varying scan rates employing a voltage range of 0 to 0.7 V. Fig. 3(a) displays the CV curves of all samples recorded at a scan rate of 3 mV s^{-1}. The voltammograms of each sample exhibit two well-defined redox peaks—corresponding to oxidation and reduction processes—appearing in both the anodic and cathodic sweeps. These peaks are indicative of faradaic redox reactions occurring at interface, highlighting the diffusion-controlled behavior of the materials. The prominent redox features confirm a redox-driven diffusion-controlled mechanism. The specific capacity (Q_s) of the electrodes is

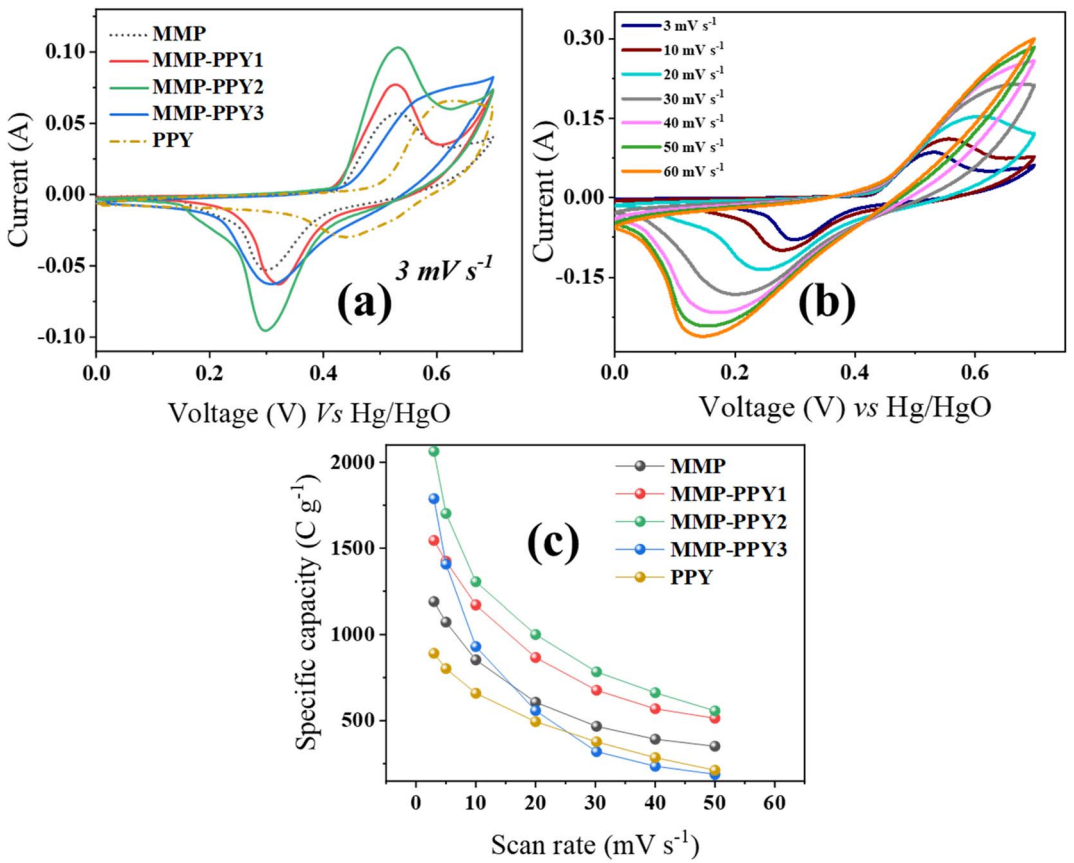

Fig. 4 (a) Comparative CV curves of all samples, (b) CV results of MMP-PPY2, and (c) Q_s calculated through CV curves.

proportional to the area enclosed by the CV loop. A comparative analysis of the voltammograms in Fig. 4(a) reveals that the MMP-PPY2 sample exhibits the largest enclosed area, signifying the highest charge storage capacity among the evaluated samples. Further insights into the rate performance of MMP-PPY2 are provided in Fig. 4(b), which presents its CV curves at various scan rates. As sweeping rate increases, the voltammograms retain their overall shape and symmetry, with broad redox peaks remaining visible. This behavior suggests excellent rate capability and electrochemical stability. The progressive shift of redox peaks with increasing scan rates is characteristic of surface-controlled redox reactions, reinforcing the redox-dominant diffusion-controlled nature of the electrode—a hallmark of high-performance, battery-type materials.

The Q_s was calculated from CV results.[52,53] As illustrated in Fig. 4(c), the electrochemical data reveal that the MMP-PPY2 composite delivers a superior specific capacity (Q_s) of 2062.6C g^{-1} at a 3 mV s^{-1} scan rate. This performance is notably higher than that of the other samples: MMP (1190.6C g^{-1}), MMP-PPY1 (1545.3C g^{-1}), MMP-PPY3 (1788.2C g^{-1}), and pure PPY (891.2C g^{-1}). The well-dispersed poly(1*H*-pyrrole) coating forms a porous, interconnected network over the MMP flakes, significantly increasing the electroactive surface area while maintaining accessible ion diffusion pathways. This balanced architecture facilitates efficient electron transport and rapid redox reactions at the electrode–electrolyte interface. Moreover, the integration of conductive PPy with the redox-active MMP matrix yields a composite that combines high capacitance, superior rate capability, and structural stability—collectively contributing to its outstanding diffusion-controlled performance.

3.2.2. Galvanostatic charge–discharge (GCD). The storage behavior was further evaluated through GCD conducted within a potential window of 0–0.6 V across varying current densities. Fig. 5(a) displays the GCD profiles of all the samples at a current density of 1.2 A g^{-1}. The discharge curves exhibit a quasi-plateau region with a distinct hump, a characteristic signature of faradaic redox processes, in good agreement with the CV observations. Among all samples, MMP-PPY2 demonstrates superior charge storage performance, reflected by its prolonged discharge time and larger integrated area under the curve. Fig. 5(b) further illustrates the GCD behavior of MMP-PPY2 across a range of current densities. The consistent retention of the redox plateau, even at higher currents, signifies excellent rate capability, coulombic efficiency (Fig. S6) and electrochemical stability. The outstanding performance of MMP-PPY2 can be attributed to its optimized composite architecture. The incorporation of 25% poly(1*H*-pyrrole) introduces a conductive and porous network that enhances electron mobility while preserving ion-accessible channels within the MMP matrix. The

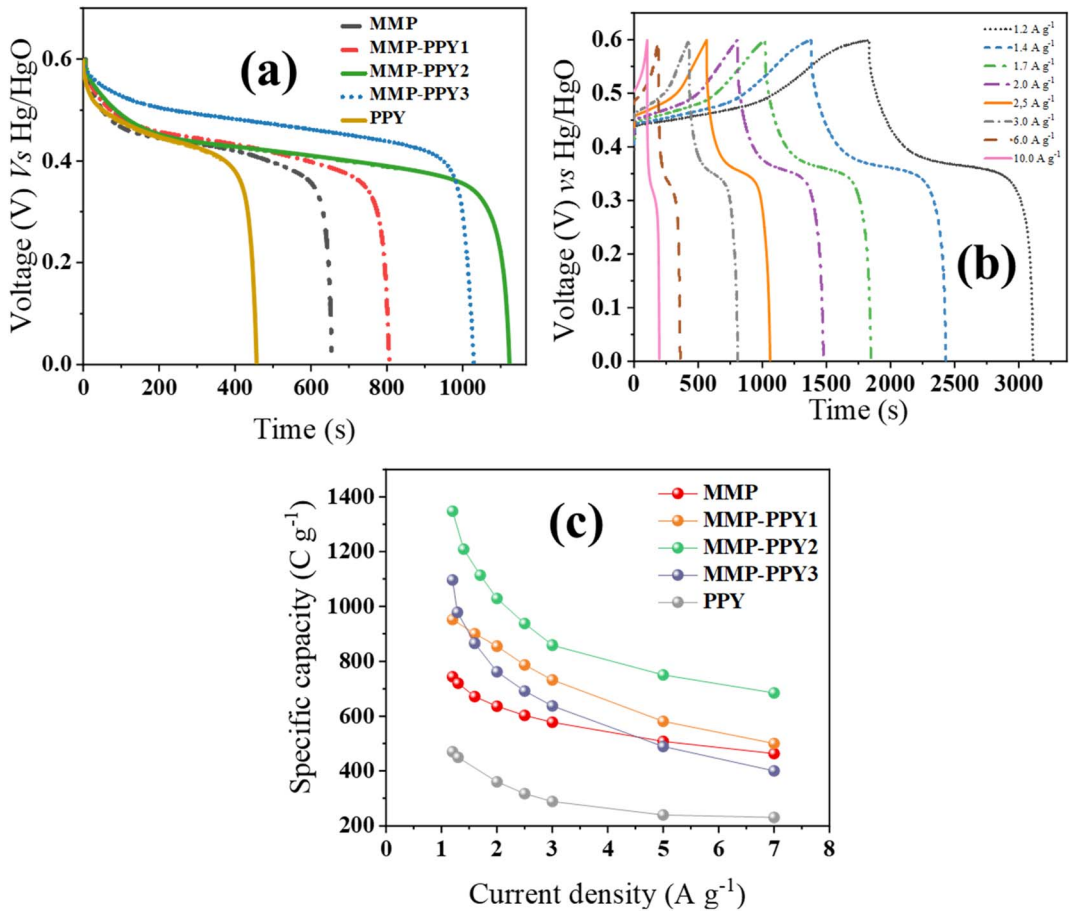

Fig. 5 (a) Discharge curves recorded at 1.2 A g^{-1} for all the samples, (b) GCD results of MMP-PPY2, and (c) Q_s calculated through GCD curves.

coulombic efficiency at 1.2 A g^{-1} was found to be around 90% (Fig. S6). The slight decrease in coulombic efficiency observed at higher current densities can be attributed to several interrelated factors. At lower current densities (1.2–3.0 A g^{-1}), the ions have sufficient time to penetrate the porous structure of the electrode, resulting in nearly complete and reversible redox reactions. However, as the current density increases (6–10 A g^{-1}), the electrochemical processes become limited by ion diffusion and charge-transfer kinetics, which restrict the full utilization of the active sites. Moreover, higher current flow induces greater internal resistance, leading to a significant IR drop and voltage polarization during charge–discharge cycles. These effects, combined with possible minor side reactions, local heating, and incomplete ion transport across the electrode–electrolyte interface, contribute to the slight decline in coulombic efficiency.

The specific capacities (Q_s) through GCD were evaluated[54] using eqn (S3) (SI section). At a current density of 1.2 A g^{-1} the samples MMP, MMP-PPY1, MMP-PPY2, MMP-PPY3, and PPY delivered 744.2, 952.1, 1347.6, 1096.2, and 470.5C g^{-1}, respectively, as depicted in Fig. 5(c). Galvanostatic charge–discharge (GCD) profiling further confirms the exceptional electrochemical behavior of the MMP-PPY2 composite. The observed reduction in specific capacity at elevated current densities occurs because of a rise in the equivalent series resistance and the electrode's restricted ability to fully integrate electrolyte ions. This limitation in ionic penetration results in slower reaction rates and a consequent rapid decrease in stored charge.[55,56]

3.2.3. Electrochemical impedance spectroscopy (EIS). The electrical conductivity and charge transfer characteristics of the phosphate-based electrodes were systematically investigated *via* EIS using 0.1 Hz to 0.1 MHz frequencies. Fig. 6 presents the Nyquist plots for all synthesized samples. The equivalent series resistance (ESR), derived from the high-frequency *x*-intercept of the plots, encompasses contributions from the intrinsic resistance of the electrode material, ion transport resistance through the KOH electrolyte, and interfacial resistance at the electrode–electrolyte boundary. The high-frequency semicircular region of the spectra reflects the charge transfer resistance, associated with electron exchange processes at the electrode surface. Notably, all samples exhibit minimal values, indicative of efficient charge transfer and good electrical conductivity. In the low-frequency region, the presence of a sloped line represents Warburg impedance (W_d), related to ion (OH^-) diffusion within the electrode structure. A steeper slope corresponds to lower ion diffusion resistance and better electrolyte accessibility. The ESR values for the analyzed samples were calculated as 1.33 Ω, 0.94 Ω, 0.68 Ω, 1.19 Ω, and 1.14 Ω, correspondingly. Among them, the MMP-PPY2 composite, with 25% PPy content, displayed the lowest ESR of 0.68 Ω. The results were fitted using the equivalent circuit. The circuit is presented in the inset, which incorporates the solution resistance (R_s) in series with a parallel branch consisting of a constant phase element (CPE) and a Warburg element (W). The Warburg component represents the ion-diffusion contribution within the porous electrode matrix. The fitted parameters corresponding to this circuit model are summarized in Table S2 (SI).

The exceptional EIS response of MMP-PPY2 can be ascribed to its well-integrated composite structure, where the conductive PPy framework not only reduces internal resistance but also facilitates rapid electron mobility and efficient ion diffusion. These features collectively position MMP-PPY2 as a highly promising electrode candidate for battery-type behavior in hybrid (asymmetric) supercapacitor systems.

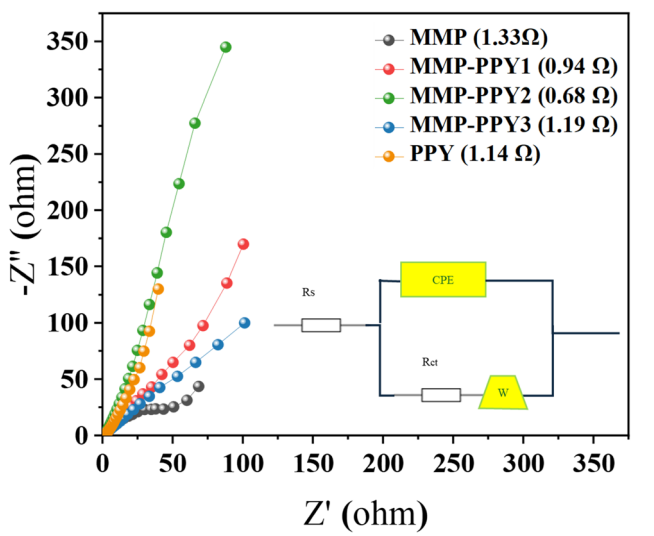

Fig. 6 Nyquist plots from electrochemical impedance spectroscopy (EIS) for all the synthesized electrode materials.

3.3. Asymmetric device

To assess the practical applicability of the MMP-PPY2 composite, an asymmetric supercapacitor device was fabricated using MMP-PPY2 as the positive electrode and activated carbon (AC) as the negative electrode, as illustrated in Fig. 7(a). Electrochemical performance of the assembled MMP-PPY2//AC device was evaluated *via* C. In a typical three-electrode configuration, AC generally operates within a voltage window of 0 to −1.0 V, while MMP-PPY2 exhibits a stable operating range of 0 to +0.7 V. Consequently, the full-cell device was assessed over an optimized operational voltage range of 0 to 1.7 V to ensure comprehensive charge storage analysis. Fig. 7(b) presents the CV curves recorded at various sweep rates. The hybrid device displays characteristic quasi-rectangular CV profiles with distinct redox features, confirming its diffusion-controlled electric double-layer hybrid behavior. Notably, the CV curves maintain their shape and symmetry even at higher scan rates, indicating excellent electrochemical stability.

Further electrochemical evaluation was carried out using galvanostatic charge–discharge (GCD) testing across a current density range of 1.9 to 14 A g^{-1} within the same potential window of 0–1.7 V. The GCD curves, shown in Fig. 7(c), exhibit non-linear features consistent with redox-based charge storage, corroborating the hybrid nature of the device. As depicted in Fig. 7(c), the asymmetric supercapacitor delivered a remarkable

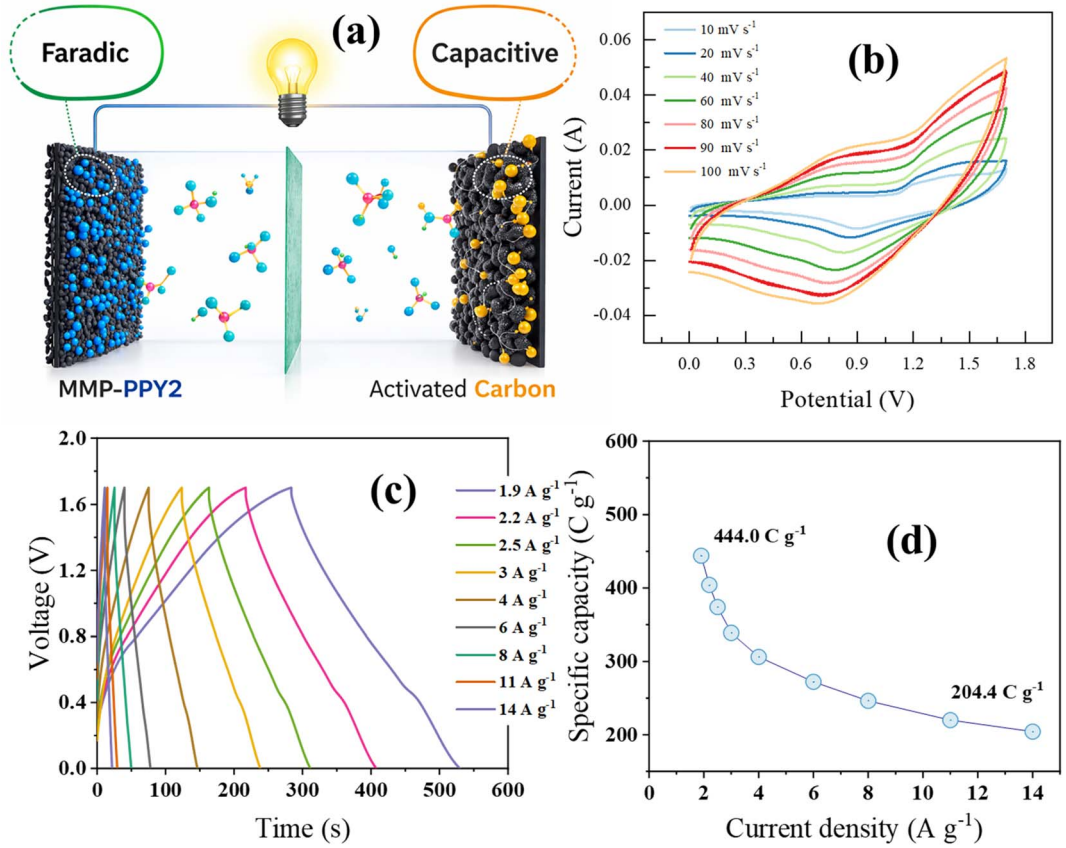

Fig. 7 (a) A schematic representation of the architecturally designed supercapacitor. (b) Cyclic voltammetry (CV) curves showing the operational characteristics of the asymmetric device. (c) Galvanostatic charge–discharge (GCD) profiles for the device. (d) Specific capacity (Q_s) values determined from the GCD data of the practical supercapacitor cell.

specific capacity of 444.0C g^{-1} at a moderate current density, while retaining 204.6C g^{-1} even at a high current load of 14 A g^{-1}—demonstrating excellent capacity retention and rate capability.

The long-term electrochemical durability of the fabricated MMP-PPY2//AC hybrid supercapacitor was assessed through cyclic stability testing over 4000 continuous GCD cycles at a high current density of 14 A g^{-1}. As presented in Fig. 8(a), the device exhibited remarkable cycling stability, retaining 97.9% of its initial charge capacity, thereby demonstrating excellent structural integrity and electrochemical resilience. The 2.1% capacity loss over 4000 cycles may be attributed to minor cumulative effects, including gradual mechanical relaxation of the PPy coating from the MMP surface during repeated volumetric changes, slight irreversible trapping of electrolyte ions within deep micropores, and marginal oxidation or restructuring of PPy chain ends under prolonged alkaline cycling. To further probe the conductivity and interfacial characteristics of the device, EIS was performed before and after cycling, using 0.1 Hz to 0.1 MHz frequency range (Fig. 8(b)) and no significant change in the spectrum is observed. The impedance spectrum revealed a low ESR of 0.60 Ω, signifying minimal internal resistance and efficient charge transport. Additionally, the charge transfer resistance was found to be nearly negligible, further confirming the superior electrochemical kinetics of the hybrid system.

Key performance indicators for energy storage devices—specific energy density (E_s) and specific power (P_s)—were also evaluated to quantify the practical potential of the hybrid supercapacitor in high-performance applications as (9).[54]

$$E_s = Q_s \times \Delta V/7.2 \quad (1)$$

$$E_s = Q_s \times 3600/\Delta t \quad (2)$$

The Ragone plot in Fig. 8(c) illustrates the overall energy-power performance of the assembled MMP-PPY2//AC asymmetric device. The device achieves a peak E_s of 104.9 Wh kg^{-1} at a power density P_s of 1615 W kg^{-1}. Furthermore, it maintains a considerable energy density of 48.4 Wh kg^{-1} even at a very high power density of 11 900 W kg^{-1}, demonstrating an excellent rate capability. This robust performance, which retains approximately 46% of its energy density as power is increased by nearly an order of magnitude, is attributed to the synergistic combination of the battery-type MMP-PPY2 cathode and the capacitive AC anode, which facilitates rapid ion transport and efficient charge transfer.

To contextualize these results, a direct comparison with recently reported asymmetric supercapacitors based on similar

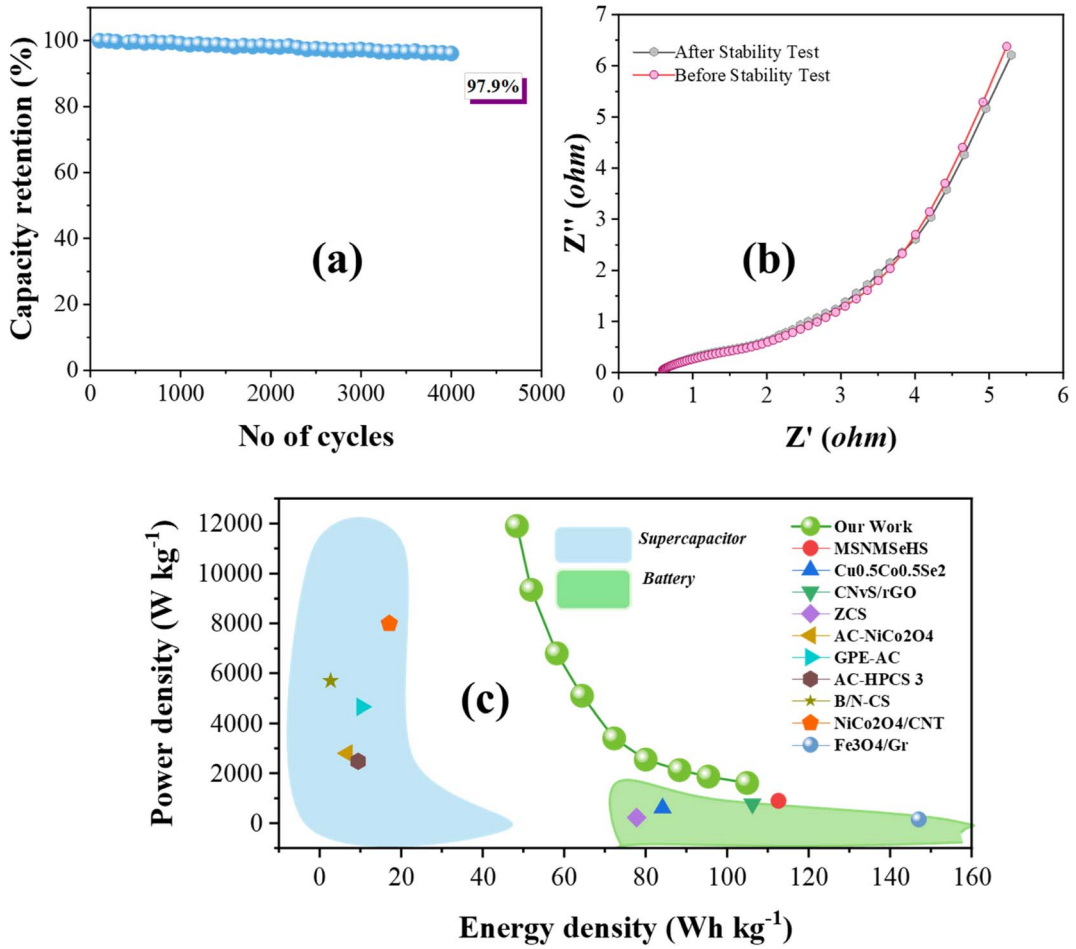

Fig. 8 (a) The measured cycling stability of the fabricated device over 4000 consecutive charge–discharge cycles. (b) EIS analysis performed on the full device. (c) A Ragone plot comparing the energy (E_s) and power (P_s) densities of the current device with previously reported systems.

materials is presented in Table 1. As evidenced by the data, the energy and power metrics of our MMP-PPY2//AC device are highly competitive, and in several key aspects, they exceed the performance of systems documented in prior studies.[57–65] We attribute this superior performance to the unique composite architecture of the MMP-PPY2 material, which offers both high pseudocapacitance and structural stability, enabling a wide operating voltage and efficient kinetics within the full device.

The *b*-value analysis was performed as shown in Fig. 9(a). The calculated *b*-values fall between 0.71 and 0.79, confirming mixed capacitive and diffusion-limited contributions.[29] Additionally, the Dunn's method was applied to separate the capacitive ($k_1\nu$) and diffusion-controlled ($k_2\nu^{1/2}$) portions of current at different scan rates employing the relation:[73]

$$I(\nu) = k_1\nu + k_2\nu^{1/2} \quad (3)$$

The k_1 and k_2 are the constants that define the capacitive and diffusion contributions, respectively, in the device's overall

Table 1 E_s and P_s obtained from MMP-PPY2//AC device compared to recently reported literature

Material	Energy density (Wh kg^{-1})	Specific power (W kg^{-1})	Ref.
MMP-PPY2//AC	104.9	1615	This work
Vanadyl phosphate/carbon/polypyrrole	30.6	813	66
NiP (surface modified)	88.03	1500	67
$CoNiP_2O_7$@PPY	94.6	1074	68
$Zn_2P_2O_7$/NF@PPybinder-free	94.2	1800	69
MnO_2/graphene/polypyrrole	22.5	4.6 K	70
LDH/PPY	86.23	973.65	71
MWCNT/NiS/PPy	33.12	6750	72

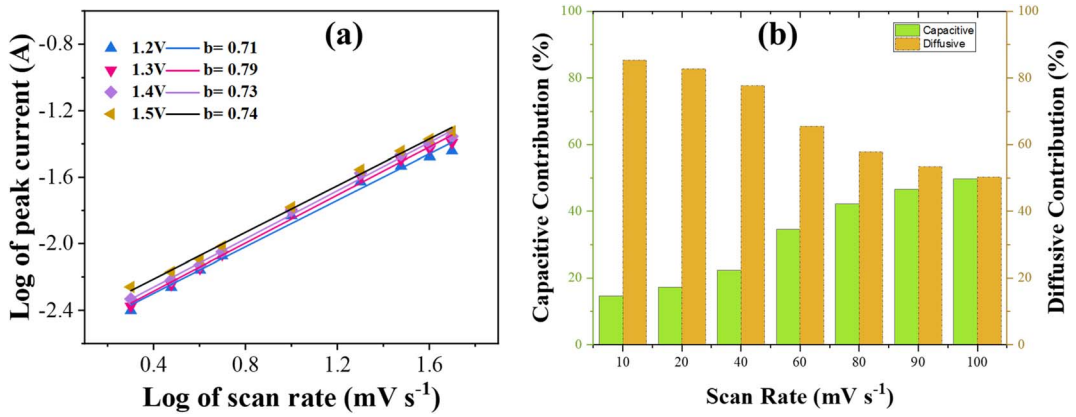

Fig. 9 (a) *b*-value analysis of real device. (b) Capacitive and diffusive contribution percentage.

performance. The quantified results (Fig. 9(b)) clearly show that both mechanisms contribute simultaneously (14.66% capacitive and 85.34% diffusion-controlled contribution at 10 mV s^{-1}), with the capacitive portion increasing at higher scan rates (49.76% capacitive and 50.24% diffusion-controlled contribution at 10 mV s^{-1}). This further affirms the hybrid potential of the fabricated device.

Additionally, the device exhibited excellent electrochemical stability, as confirmed by a leakage current test conducted by holding it at the maximum operating voltage of 1.7 V for 12 hours, during which no measurable leakage current was observed. The internal resistance of the device, determined from the IR drop during galvanostatic charge–discharge measurements, was found to be 0.03 V, indicating low internal resistance and efficient charge transfer. These results support the reported high energy density of 104.9 Wh kg^{-1} and validate the performance of the device under the given operating conditions.

4. Conclusion

In this study, a mixed-metal phosphate (MMP) and poly(1*H*-pyrrole) (PPy) were combined using a straightforward physical mixing method. Morphological and structural analyses confirmed the successful formation and uniform integration of the composite materials. Electrochemical evaluation in a three-electrode configuration revealed that the MMP-PPY2 (25 wt% poly(1*H*-pyrrole)) composite exhibited the highest specific capacities among all samples, achieving 1347.6C g^{-1} at a current density of 1.2 A g^{-1}. The optimized MMP-PPY2 electrode was further assembled into an asymmetric supercapacitor (MMP-PPY2//AC) that delivered outstanding performance, attaining a high specific energy of 104.9 Wh kg^{-1}, alongside a specific power of 1615 W kg^{-1}. Impressively, the device retained 48.4 Wh kg^{-1} of energy while delivering a 11 900 W kg^{-1} power density. In addition, the device exhibited exceptional long-term stability, maintaining 97.9% of its initial capacity after 4000 continuous cycles. These results underscore the effectiveness of incorporating conductive PPy into the MMP matrix, significantly enhancing electrochemical performance through improved charge transport and ion diffusion pathways. The binary MMP-PPY2 composite demonstrates great potential as a high-performance electrode material for next-generation asymmetric supercapacitor applications.

Conflicts of interest

The authors declare no conflict of interest.

Data availability

The data will be made available on request.

Supplementary information (SI) is available. See DOI: https://doi.org/10.1039/d6ra02421a.

Acknowledgements

The authors would like to acknowledge Ongoing Research Funding Program, (ORF-2026-43), King Saud University, Riyadh, Saudi Arabia.

References

1 Z. Abdin, *J. Energy Storage*, 2024, **86**, 111354.
2 R. Khalid, A. Shah, M. Javed and H. Hussain, *RSC Adv.*, 2025, **15**, 15951–15998.
3 A. G. Olabi, Q. Abbas, A. Al Makky and M. A. Abdelkareem, *Energy*, 2022, **248**, 123617.
4 K. Dissanayake and D. Kularatna-Abeywardana, *J. Energy Storage*, 2024, **96**, 112563.
5 S. M. Mousavi, S. A. Hashemi, M. Y. Kalashgrani, A. Gholami, M. Binazadeh, W.-H. Chiang and M. M. Rahman, *Sustain. Energy Fuels*, 2023, **7**, 5176–5197.
6 A. Tundwal, H. Kumar, B. J. Binoj, R. Sharma, G. Kumar, R. Kumari, A. Dhayal, A. Yadav, D. Singh and P. Kumar, *RSC Adv.*, 2024, **14**, 9406–9439.
7 R. S. Karmur, D. Gogoi, M. R. Das and N. N. Ghosh, *RSC Adv.*, 2024, **14**, 27465–27474.
8 J. Riaz, J. Cao, Y. Zhang, A. Bibi and X. Zhou, *Nanoscale Adv.*, 2024, **6**, 5145–5157.

9 P. N. Thonge, S. D. Dhas, S. D. Waghmare, A. H. Patil, T. M. Patil, M. A. Yewale, A. C. Mendhe and D. Kim, *ACS Appl. Nano Mater.*, 2024, **7**, 18579–18589.
10 H. Hegazy, J. Khan, N. Shakeel, E. A. Alabdullkarem, M. I. Saleem, H. Alrobei and I. Yahia, *RSC Adv.*, 2024, **14**, 32958–32977.
11 M. Vandana, K. Bijapur, G. Soman and G. Hegde, *Crit. Rev. Solid State Mater. Sci.*, 2024, **49**, 335–370.
12 M. Ali and A. Gherissi, *J. Ceram. Process. Res.*, 2019, **20**, 259–263.
13 P. K. Sahoo, N. Kumar, A. Jena, S. Mishra, C.-P. Lee, S.-Y. Lee and S.-J. Park, *RSC Adv.*, 2024, **14**, 1284–1303.
14 S. V. Sadavar, S. Y. Lee and S. J. Park, *Advanced Science*, 2024, **11**, 2403172.
15 A. Aldayyat and F. K. Yam, *J. Solid State Electrochem.*, 2025, **1–32**, 4249–4280.
16 M. Saqib, A. Asghar, Z. Chen, A. A. A. Hafez, M. Y. Almashnowi, Q. Arshad, M. Y. Awaji, Y. Javad, M. Kuku and M. S. Rashid, *J. Alloys Compd.*, 2025, **1010**, 177986.
17 R. I. Mohanty, A. Mukherjee, P. Bhanja and B. K. Jena, *J. Energy Storage*, 2024, **80**, 110313.
18 A. Samal, C. Mohanty, N. Das, R. Das and M. F. Kühnel, *Mater. Today Chem.*, 2024, **38**, 102096.
19 A. C. Mendhe, A. Kore, S. D. Dhas, Y. Kim, R. Batool, A. Ghazal and D. Kim, *Chem. Eng. J.*, 2024, **489**, 151168.
20 V. Thirumal, B. Babu, J. Kim, K. Yoo and S. H. Lee, *J. Alloys Compd.*, 2025, **1022**, 179956.
21 M. Subbiah, Z. M. Almarhoon, A. Mariappan, S. Venkatachalam, S. Pitchaimuthu and N. Srinivasan, *Electrochim. Acta*, 2024, **498**, 144644.
22 M. Ali, *Open Eng.*, 2024, **14**, 20240063.
23 T. Yang, Y. Yan, R. Liu, K. Huang, R. Xu, J. Chen, J. Tu, S. Liu, L. Kang and Z. Wang, *Nano Lett.*, 2025, **25**, 7707–7715.
24 N. L. W. Septiani, S. Chowdhury, A. Hardiansyah, M. Rinawati, M.-H. Yeh, H. Nara, Y. Yamauchi, Y. V. Kaneti and B. Yuliarto, *J. Mater. Chem. A*, 2024, **12**, 14045–14058.
25 C. Chavare, D. S. Sawant, S. Gaikwad, A. V. Fulari, H. Kulkarni, D. P. Dubal and G. M. Lohar, *J. Mater. Chem. A*, 2025, 6993–7054.
26 V. V. Patil, N. Kumar, R. R. Salunkhe, J. L. Gunjakar, C. D. Lokhande, M. G. Mali, V. G. Parale, H.-H. Park, D. S. Mhamane and U. M. Patil, *Chem. Eng. J.*, 2024, **485**, 150055.
27 P. K. Katkar, Z. A. Sheikh, V. D. Chavan and S.-W. Lee, *J. Mater. Sci. Technol.*, 2025, **206**, 282–296.
28 M. M. Faisal, S. R. Ali, M. Z. Iqbal, M. W. Iqbal, A. Numan and K. Sanal, *J. Energy Storage*, 2021, **44**, 103329.
29 J. Khan, N. Shakeel, M. Z. Iqbal and A. A. Al-Kahtani, *J. Energy Storage*, 2024, **81**, 110432.
30 M. Z. Iqbal, J. Khan, H. T. A. Awan, M. Alzaid, A. M. Afzal and S. Aftab, *Dalton Trans.*, 2020, **49**, 16715–16727.
31 A. A. Kulkarni, N. K. Gaikwad, A. P. Salunkhe, R. M. Dahotre and T. S. Bhat, *J. Electroanal. Chem.*, 2023, **948**, 117795.
32 S. S. Patil and P. S. Patil, *Chem. Eng. J.*, 2023, **455**, 140639.
33 M. Ali, *Int. J. Chem. Molecul. Nucl. Mater. Metall. Eng*, 2016, **10**, 234–240.
34 B. G. Thali, D. S. Agrahari and R. M. Kamble, *ChemistrySelect*, 2025, **10**, e202502298.
35 Z. Chen, Y. Wang, M. Wang, F. Yong, W. Luo, M. Zhao and F. Yu, *ACS Appl. Nano Mater.*, 2023, **6**, 7465–7476.
36 A. Kumar, P. Kumar, S. K. Soni, M. L. Verma and G. Dixit, *Electrochim. Acta*, 2026, 148445.
37 S. Alam, S. Jadoon, M. Z. Iqbal, H. H. Hegazy, Z. Ahmad and I. S. Yahia, *J. Energy Storage*, 2024, **85**, 110955.
38 V. V. Vinayak, K. Deshmukh, V. Murthy and S. K. Pasha, *J. Energy Storage*, 2024, **100**, 113551.
39 A. Zheng, C. Tao, J. Guo, Z. Shi, X. Cao, Z. Zhang and X. Yang, *Chem. Eng. J.*, 2025, **516**, 164116.
40 L. Hao and D. Yu, *Synth. Met.*, 2022, **290**, 117138.
41 M. Ali, *Rev. Adv. Mater. Sci.*, 2023, **62**, 20230126.
42 O. B. Abdillah, Y. B. Rus, M. Ulfa and F. Iskandar, *J. Energy Storage*, 2023, **74**, 109300.
43 S. Meenakshy, J. Jesslyn and S. Anas, *Adv. Mater. Technol.*, 2025, **10**, 2401216.
44 S. Pavithra, R. Thejas, H. A. Rao, B. Krishna and G. Nagaraju, *Macromol. Res.*, 2024, **32**, 23–33.
45 Y. He, Z. Fan, P. Sun, H. Jiang, Z. Chen, G. Tang, Z. Hou, Y. Sun, Y. Yi and W. Shi, *Small Methods*, 2024, **8**, 2301405.
46 Y. Yan, B. Wang, P. Li, B. Qin, Z. Ye, Y. Xia, Z. Zhang, Z. Wang, Y. Li and X. Zheng, *Trans. Mater. Res. Soc. Jpn*, 2025, **1**, 100038.
47 L. Zhou, Q. Liu, X. Ma, P. Sun, X. Lv, L. Fang, X. Sun and M.-H. Shang, *Chem. Eng. J.*, 2022, **450**, 138035.
48 M. Vinitha and G. Velraj, *J. Mater. Sci.: Mater. Electron.*, 2022, **33**, 6627–6635.
49 S. Ansari, S. Kumar, D. Nayak, G. Mandal, J. Bauri and R. B. Choudhary, *Mater. Today: Proc.*, 2024, **127**, 82–87.
50 X. Liang, Y. Liu, Z. Wen, L. Huang, X. Wang and H. Zhang, *J. Power Sources*, 2011, **196**, 6951–6955.
51 X. Liang, Z. Wen, Y. Liu, X. Wang, H. Zhang, M. Wu and L. Huang, *Solid State Ionics*, 2011, **192**, 347–350.
52 A. Ahmed, M. R. Abdul Karim and M. Usman, *Energy Technol.*, 2025, 2401761.
53 A. Ahmed, M. R. A. Karim and M. Usman, *Electrochim. Acta*, 2025, 145764.
54 A. Ahmed, M. R. A. Karim and M. Usman, *Electrochim. Acta*, 2025, **531**, 146351.
55 Y. Shao, M. F. El-Kady, J. Sun, Y. Li, Q. Zhang, M. Zhu, H. Wang, B. Dunn and R. B. Kaner, *Chem. Rev.*, 2018, **118**, 9233–9280.
56 E. Mourad, L. Coustan, P. Lannelongue, D. Zigah, A. Mehdi, A. Vioux, S. A. Freunberger, F. Favier and O. Fontaine, *Nat. Mater.*, 2017, **16**, 446–453.
57 A. Izadi-Najafabadi, S. Yasuda, K. Kobashi, T. Yamada, D. N. Futaba, H. Hatori, M. Yumura, S. Iijima and K. Hata, *Adv. Mater.*, 2010, **22**, E235–E241.
58 F. Zhang, T. Zhang, X. Yang, L. Zhang, K. Leng, Y. Huang and Y. Chen, *Energy Environ. Sci.*, 2013, **6**, 1623–1632.
59 Y.-W. Chi, C.-C. Hu, H.-H. Shen and K.-P. Huang, *Nano Lett.*, 2016, **16**, 5719–5727.
60 T. Shang, Y. Xu, P. Li, J. Han, Z. Wu, Y. Tao and Q.-H. Yang, *Nano energy*, 2020, **70**, 104531.

61 B. Song, J. Zhao, M. Wang, J. Mullavey, Y. Zhu, Z. Geng, D. Chen, Y. Ding, K.-s. Moon and M. Liu, *Nano Energy*, 2017, **31**, 183–193.
62 X. Wang, A. Y. Mehandzhiyski, B. Arstad, K. L. Van Aken, T. S. Mathis, A. Gallegos, Z. Tian, D. Ren, E. Sheridan and B. A. Grimes, *J. Am. Chem. Soc.*, 2017, **139**, 18681–18687.
63 T. Kim, G. Jung, S. Yoo, K. S. Suh and R. S. Ruoff, *ACS Nano*, 2013, **7**, 6899–6905.
64 K. H. Lee, Y.-W. Lee, S. W. Lee, J. S. Ha, S.-S. Lee and J. G. Son, *Sci. Rep.*, 2015, **5**, 13696.
65 X. Yang, C. Cheng, Y. Wang, L. Qiu and D. Li, *science*, 2013, **341**, 534–537.
66 N. Chen, J. Zhou, G. Zhu, Q. Kang, H. Ji, Y. Zhang, X. Wang, L. Peng, X. Guo and C. Lu, *Nanoscale*, 2018, **10**, 3709–3719.
67 A. Asghar, M. S. Rashid, S. Hussain, Y. Javed and Z. Chen, *Mater. Chem. Phys.*, 2025, 131038.
68 S. Sathishkumar, M. Karthik, R. Boopathiraja, S. Nirmaladevi, M. Ouladsmane, T. Niyitanga and H. Kim, *Energy Technol.*, 2024, **12**, 2301589.
69 M. Premkumar, S. Radjarejesri, S. Vadivel and O. H. Abd-Elkader, *Ionics*, 2025, **31**, 781–798.
70 S. Ye, A. Xu, W. Cao, Z. Zhao, S. Zhang and Y. Qin, *Langmuir*, 2024, **40**, 11460–11469.
71 Y. Wu, X. Liu, J. Wang, B. Zhang, X. Zhang and O. Hai, *J. Energy Storage*, 2025, **110**, 115295.
72 A. Baby, J. Vigneswaran, S. P. Jose, D. Davis and S. PB, *Mater. Today Sustain.*, 2024, **26**, 100727.
73 M. Arslan-Kaba, S. Timur and G. K. Sireli, *J. Energy Storage*, 2024, **99**, 113299.